ACS OMEGA

http://pubs.acs.org/journal/acsodf
Article

Combustion-Controlled Thermal Loading and Non-Isothermal Spinel Growth in $MgO-Al_2O_3$ Systems under Premixed Strained Syngas/Air Flames

Chunkan Yu,* Sanchita Chakrabarty, and Michael Fischlschweiger

Cite This: https://doi.org/10.1021/acsomega.6c05832

ABSTRACT: High-temperature solid-state reactions are highly sensitive to thermal loading, requiring precise control of temperature magnitude and evolution. In the present work, a thermodynamically consistent multiscale framework is developed to simulate nonisothermal solid-state reactions induced by a laminar strained premixed CO/H_2/air flame. The thermal field within a $MgO-Al_2O_3$ material system is controlled through modulation of the imposed flame strain rate, while the growth kinetics of magnesium aluminate spinel ($MgAl_2O_4$) are described using a Thermodynamic Extremal Principle (TEP)-based non-equilibrium model coupled to CALPHAD. The results show that decreasing the flame strain rate provides an effective and physically possible strategy to regulate the internal material temperature under homogeneous conditions. Different flame strain-rate transition times lead to different heating profiles and significantly influence the evolution of spinel thickness. Faster heating results in thinner spinel layers despite higher instantaneous growth rates, which are attributed not only to temperature-dependent diffusion but also to enhanced thermodynamic driving forces arising from the expansion of the spinel stability region at elevated temperatures. Stochastic fluctuations in the flame strain rate are shown to have negligible impact on the material temperature evolution due to thermal inertia, indicating robustness of the proposed thermal control strategy. The proposed framework establishes a direct link between controllable combustion parameters and solid-state reaction, providing a foundation for combustion-driven thermal engineering of advanced ceramic systems.

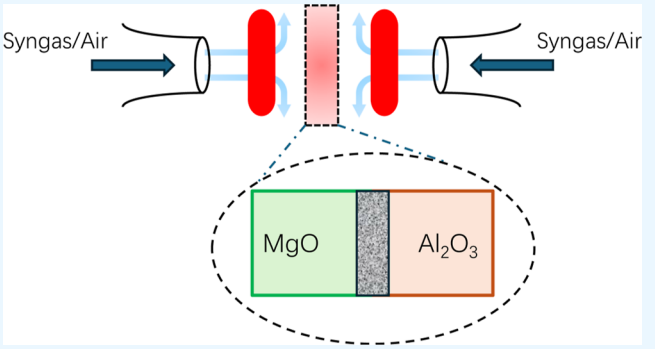

INTRODUCTION

Solid-state reactions play a central role in a wide range of high-temperature material processing and synthesis routes for functional oxide layers that involves multiple kinetics such as diffusion and interfacial reactions. These processes are highly sensitive to temperature, not only in terms of the achievable reaction rates but also with respect to microstructural evolution and phase stability. Precise control of the thermal history of the material is therefore essential to ensure reproducibility and to avoid undesired phase transformations or material degradation.[1,2]

Among the available high-temperature heat sources, combustion systems provide an attractive means of supplying the high temperatures required for solid-state reactions, owing to their ability to deliver intense heat fluxes with relatively simple system configurations. Compared to alternative heating methods such as electrical or plasma-based systems, combustion-based approaches offer high energy density, scalability, and operational flexibility,[3−5] making them particularly suitable for applications requiring sustained high-temperature environments.

From an energy engineering perspective, the capability to control the spatial and temporal distribution of temperature is a key requirement for advanced thermal processes.[6−8] Modern combustion systems allow such control through adjustments of operating parameters such as fuel composition, equivalence ratio, and flow conditions. In well-defined flame configurations, these parameters can be tuned to regulate flame temperature and heat transfer to adjacent solid materials, enabling precise thermal management rather than merely maximum heat release. As a result, combustion remains a relevant and versatile technology for high-temperature energy applications, particularly when combined with low-carbon fuels such as syngas or hydrogen-rich mixtures.[9−11] Laminar strained premixed flame is one of the well-defined flame configuration,

Received: May 20, 2026
Revised: July 17, 2026
Accepted: August 11, 2026

which offers a well-defined and highly controllable configuration for fundamental and practical application of combustion and heat transfer. Owing to their symmetric flow field and clearly defined stagnation plane, key parameters such as strain rate or flow velocity can be precisely prescribed and systematically varied.[12−14] This well-characterized structure enables a direct link between imposed flow conditions and the resulting flame behavior, which is essential for reproducible investigations of flame−material interactions.[15,16]

In the context of ongoing energy transitions, combustion technologies are also shifting toward cleaner and more sustainable fuel pathways.[11,17,18] The use of alternative fuels, such as syngas, hydrogen-rich mixtures, or fuels derived from renewable feedstocks, extends the applicability of combustion to low-carbon or zero-carbon energy systems. For example, hydrogen combustion has been considered a potential energy carrier for glass manufacturing to support large-scale decarbonization efforts,[19] and the associated increase in water vapor within the furnace atmosphere introduces additional considerations regarding glass chemistry and properties, which have been discussed in detail. In ref 20 green ammonia cofiring was evaluated as an alternative fuel for the cement industry to supply the thermal energy required for rotary kilns. The corresponding NO_x emissions during cement production were investigated in detail, and the quality of the produced cement was systematically assessed.

In the present work, the formation of Magnesium aluminate spinel ($MgAl_2O_4$) through the solid-state reaction between MgO and Al_2O_3 under high-temperature contact conditions is investigated. The required thermal energy is supplied by a syngas-fueled combustion system, where a premixed mixture of CO and H_2 serves as the energy source. By applying combustion as the heating mechanism, controlled high-temperature environments can be established, enabling systematic investigation of diffusion-controlled phase formation at ceramic interfaces. Magnesium aluminate spinel ($MgAl_2O_4$) is of considerable industrial importance due to its excellent thermo-mechanical stability, high melting point, superior chemical inertness, and relatively low thermal expansion coefficient.[21−24] These properties make spinel-based materials attractive for applications in high-temperature structural components, transparent ceramics and thermal barrier systems for this material. In addition, the compatibility of spinel with both MgO- and Al_2O_3-rich environments further enhances its relevance in multiphase ceramic assemblies. Understanding the kinetics of spinel formation under well-defined and externally controllable thermal conditions is therefore of both scientific and technological significance. In this context, coupling combustion-controlled thermal loading with solid-state reaction modeling provides a novel framework to analyze the interaction between flame dynamics and magnesium aluminate spinel formation.

MATHEMATICAL MODELING AND SIMULATION

Before presenting the mathematical formulation in detail, the physical configuration considered in the present study is first described, as illustrated in Figure 1. The system consists of two solid plates made of periclase (per, MgO) and corundum (cor, Al_2O_3), respectively, which are brought into contact through a polished interface. The two plates are assumed to have identical thickness δ and are placed symmetrically at the stagnation plane of a laminar strained premixed CO/H_2/air flame. At the initial stage ($t = 0$ in the figure), the entire system

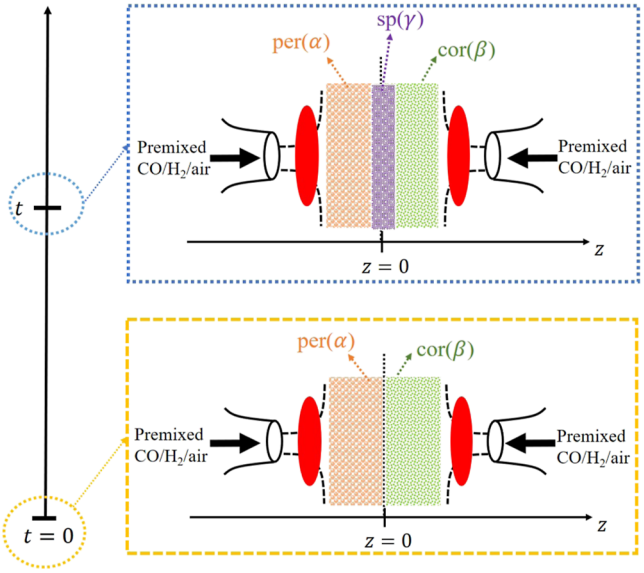

Figure 1. Schematic illustration of spinel (sp) growth as an interlayer formation between periclase (per) and corundum (cor) system during the temperature variation at material surface caused by strained laminar premixed CO/H_2/air flame.

is assumed to be in thermodynamic equilibrium, such that the temperature within the solid material is spatially homogeneous. Under this condition, no temperature gradient exists either inside the solid or at the interface between the solid surface and the flame regime.

As reported in the literature,[25] when a uniaxial thermal load is applied to the two plates using a creep apparatus, diffusion and chemical reactions between the periclase and corundum phases lead to the formation of a thin spinel (sp) layer at the interface, as schematically indicated at time t in the Figure 1. The formation and growth of this spinel layer are strongly temperature dependent. Therefore, by controlling the thermal state of the system through adjustments of flame parameters (such as the imposed flame strain rate and the composition of the unburnt mixture), the material temperature can be effectively regulated. This temperature control capability provides a direct means to influence the interfacial reactions and phase evolution within the solid during the process.

Laminar Strained Premixed Flame

Thermo-Kinetic and Fluid Dynamics Quantities. In the present study, the thermo-kinetic and fluid-dynamic state of the strained premixed flame is described using the two-parameter formulation,[26] in which the full two-dimensional (2D) reacting flow can be reduced to a one-dimensional (1D) representation along the axial coordinate z (c.f. Figure 1). Within this framework, all governing equations are expressed as functions of z and time t, while the effects of the transverse flow (in radial direction) are captured through two independent quantities, namely the tangential velocity gradient $G(z, t) = \frac{v_x(z,t)}{r}$ and the tangential pressure gradient $J = -\frac{1}{r}\frac{\partial p_g}{\partial r}$, where v_r denotes the radial velocity component of gas mixture. The resulting two-parameter (introduction of G and J) formulation allows the conservation equations to depend solely on z and t. In the following formulation, subscripts "$_g$" are used to denote quantities associated with the gas-phase flame.

https://doi.org/10.1021/acsomega.6c05832
ACS Omega XXXX, XXX, XXX−XXX

The thermodynamic state of the mixture is characterized by the gas-phase temperature $T_g(z, t)$, the pressure p_g and the density ρ_g. Chemical composition is described by the species mass fractions $w_i(z, t)$, whose evolution is governed by chemical source terms $\dot{\omega}_i$. These source terms are evaluated from elementary reaction kinetics, with rate coefficients following the Arrhenius law.[27−29]

Governing Equations. For clarity, a brief summary of the governing equations is provided below. Although the two-parameter formulation has been presented in detail elsewhere,[26] several components are restated because they play a central role in modeling flame−material heat transfer and in defining the interface boundary conditions introduced later. Consistent with the reduction described in the previous subsection, the reacting flow is represented as a one-dimensional system along the axial coordinate z and the full governing conservation equations reduce to the following one-dimensional form[26]

$$\frac{\partial \rho_g}{\partial t} = -2\rho_g G - \frac{\partial(\rho_g v_z)}{\partial z} \tag{1}$$

$$\frac{\partial G}{\partial t} = -\frac{J}{\rho_g} - G^2 + \frac{1}{\rho_g}\frac{\partial}{\partial z}\left(\eta_g \frac{\partial G}{\partial z}\right) - v_z \frac{\partial G}{\partial z} \tag{2}$$

$$\frac{\partial T_g}{\partial t} = -\frac{1}{\rho_g c_{p,g}}\frac{\partial}{\partial z}\left(-\lambda_g \frac{\partial T_g}{\partial z} + T_g \sum_{i=1}^{n_s} c_{pi} j_{i,g}\right) - \frac{1}{\rho_g c_{p,g}} \sum_{i=1}^{n_s} \dot{\omega}_i \bar{h}_i - v_z \frac{\partial T_g}{\partial z} \tag{3}$$

$$\frac{\partial w_i}{\partial t} = -\frac{1}{\rho_g}\frac{\partial j_{i,g}}{\partial z} + \frac{\dot{\omega}_i M_i}{\rho_g} - v_z \frac{\partial w_i}{\partial z} \tag{4}$$

$$0 = \rho_g - \frac{p_g \bar{M}}{R T_g} \tag{5}$$

In these equations, η_g represents dynamic viscocity, $c_{p,g}$ the isobaric heat capacity, λ_g the heat conductivity, $\bar{M}$ the mean molar mass of the mixture and R the universal gas constant. Each species i contains the thermo-kinetic information regarding the isobaric heat capacity $c_{p,i}$, molar mass M_i and molar enthalpies $\bar{h}_i$. Mass transport is captured through the multicomponent diffusion fluxes $j_{i,g}$ which include differential molecular diffusion involving mass diffusion coefficient D_i^d and thermal diffusion involving the thermal diffusion coefficient D_i^T

$$j_{i,g} = -\rho_g D_i^d \frac{w_i}{x_i}\frac{\partial x_i}{\partial z} - \frac{D_i^T}{T_g}\frac{\partial T_g}{\partial z} \tag{6}$$

Here x_i is the mole fraction of i-th species. Both D_i^d and D_i^T are calculated according to ref 30.

It should be explicitly mentioned that the objective of the current work is not to perform a sensitivity analysis of individual combustion submodels, but rather to investigate how a combustion-controlled thermal field influences the evolution of spinel growth in a coupled flame−material system. For this reason, detailed transport and chemistry models, including differential diffusion of different species, thermal diffusion (Soret effect) and surface reactions, were incorporated to represent the flame environment as realistically and consistently as possible under high-temperature conditions. The influence of individual combustion effects, such as the Soret effect, on strained premixed flames has already been extensively discussed in the combustion literature.[31−33] Therefore, a separate systematic assessment of these effects is beyond the scope of the present study. Instead, these detailed submodels are included here to improve the physical fidelity of the thermal boundary conditions supplied to the solid-state reaction model.

Solid-State Reaction Based on Thermodynamic Extremal Principle

The solid state synthesis of Magnesium aluminate spinel (MAS) from MgO and Al_2O_3, as shown in Figure 1, depends on both the temperature of the applied flame and the exposure time of the system. The thickness, as well as the composition of the formed product layer of MAS can be tailored by controlling the applied temperature−time profile. To explore such process-structure relationship, the growth kinetics of the MAS, in dependence of the temperature change induced by combustion system, has been included in this work by implementing the kinetic model that has been developed in.[25,34] The developed model is based on the nonequilibrium thermodynamic concept of the Thermodynamic Extremal Principle (TEP) that has proved to be a valuable tool for the systematic development of evolution equations, capturing the complex kinetic phenomena occurring in multicomponent, multiphase material systems.[35,36]

Brief Outline of Governing Equations. The multiple internal kinetics that have been taken into account for this particular solid state reaction system are that of the bulk diffusion; the diffusion of Al_2O_3 through the spinel to the MgO side for further reaction and that of the MgO to the Al_2O_3 side, the interface migration; the movement of the MgO/spinel and spinel/Al_2O_3 interfaces into the MgO and Al_2O_3 phases respectively and finally the vacancy generation/annihilation at these respective reaction interfaces.[34] Each of these kinetic processes dissipate the Gibbs energy of the overall system, the rate of which has been presented as[25]

$$\dot{G} = \frac{g_\alpha}{\Omega_\alpha}u_\alpha + \frac{g_\beta}{\Omega_\beta}v_\beta + \frac{1}{\Omega_\gamma}\left[-v_\gamma g_\gamma(r_L) + u_\gamma g_\gamma(r_R) + \int_{X_L}^{X_R}\frac{dg_\gamma}{dr}\dot{r}\,dx\right] \tag{7}$$

where the Gibbs energies of each of the per/α/MgO, cor/Al_2O_3 and sp/γ/spinel phases are represented by g_α, g_β and g_γ. The MgO and Al_2O_3 being stoichiometric compounds, g_α and g_β are only temperature dependent. However, since spinel is a solid solution, g_γ varies both with respect to temperature and composition. Following the works in,[25,34,37] the spinel composition, in terms of the mole fraction of Al_2O_3, represented here as r, is assumed to have a linear profile within the spinel (position coordinate being denoted by x), with the left (L)and right (R) boundary values (at per/sp and sp/cor interfaces) represented as r_L and r_R respectively. The velocity with which the left interface moves with respect to each of the α and γ phase lattices has been further denoted by u_α and v_γ respectively. v_β and u_γ represent the velocity of the right interface with respect to the lattices of the β and γ phases. Ω_α, Ω_β and Ω_γ represent the molar volumes of the

https://doi.org/10.1021/acsomega.6c05832
ACS Omega XXXX, XXX, XXX−XXX

corresponding phases. For further in-depth derivation of eq 7, the reader can refer to ref 25.

According to the principles of irreversible thermodynamics, for a closed system, this rate of Gibbs energy dissipation equates to the negative of the dissipation rate Q of the system.[25] Subject to this constraint, the TEP principle maximizes Q with respect to the kinetic variables that on the one hand can be used to physically design the expressions for $\dot{G}$ and Q and on the other hand, are important to characterize the system evolution over time.[25,34,35,38] The final expression from the constrained maximation of TEP is given as[39]

$$-\frac{1}{2}\sum_i \frac{\partial^2 Q}{\partial J_i \partial J_i} J_i = \frac{\partial \dot{G}}{\partial J_i} \tag{8}$$

where J_i represents here the kinetic variables (u_α, v_γ, v_β, u_γ, $\dot{r}_L$ and $\dot{r}_R$), that have been used to represent $\dot{G}$ in eq 7, and is further shown to form the expression for Q. It constitutes the contributions of the dissipation rate from each of the processes of diffusion Q_d, interface migration Q_m and vacancy generation/annihilation $Q_{a/g}$ as is represented as[25]

$$Q = Q_d + Q_m + Q_{a/g} \tag{9}$$

The term describing the process of diffusion Q_d is expressed as[25]

$$Q_d = R_g T \Omega_\gamma \int_{X_L}^{X_R} \left(\frac{j_A^2}{(1-r)D_A} + \frac{j_B^2}{rD_B} \right) dx \tag{10}$$

where R_g is the universal gas constant, T the system temperature at each time instance as is obtained from the flame calculation, j_A and j_B are the mass fluxes of MgO and Al_2O_3 through the spinel respectively due to the diffusion process. D_A and D_B are the diffusion coefficients of the effective components MgO and Al_2O_3 in the spinel respectively that show a temperature dependence according to the Arrhenius's law.

The dissipation rate from the interface migration Q_m is given as[25]

$$Q_m = \frac{(u_\alpha + v_\gamma)^2}{4M_L} + \frac{(u_\gamma + v_\beta)^2}{4M_R} \tag{11}$$

in which M_L and M_R are the mobility coefficients of the left and right interfaces. Similar to the diffusion coefficients, they follow the Arrhenius's law and the corresponding coefficient parameters are derived from.[34]

Finally, the expression for $Q_{a/g}$ is given as[25]

$$Q_{a/g} = \frac{(v_\gamma - u_\alpha)^2}{U_L} + \frac{(v_\beta - u_\gamma)^2}{U_R} \tag{12}$$

where U_L and U_R are the vacancy generation/annihilation coefficients for the left and right interfaces. These values are assumed to be kept constant due to its lower influence compared to diffusion and interface migration[34] on this specific solid state transformation within the specific temperature window studied. For further detailed knowledge of the equations, the reader might refer to.[25,34]

Flame-Material Interface Boundary Condition

In this section, the boundary conditions imposed at the flame−material interface are specified in detail. Accurate formulation of these conditions is essential, as the coupling between the reacting flow and the solid material involves both heat and mass transfer processes. The position of the flame−material interface is denoted by I, with I^- referring to the material side and I^+ to the gas-phase flame side. It should be emphasized that, in the present framework, the combustion system is considered solely as a thermal energy source for the solid-state reaction. Apart from the heterogeneous surface reactions considered at the flame−material interface, no transport of gas-phase species into the solid material is considered. Consequently, possible effects associated with hydrogen diffusion, radical penetration, or other combustion-product-assisted reactions within the material are neglected and are not included in the modeling at the flame-material interface.

Species Mass Transport

With respect to species mass transport, the solid material is assumed to be impermeable to all gas-phase species. Consequently, no net mass transfer across the interface into the solid is allowed. However, heterogeneous surface reactions are permitted to occur at the material surface. Under these assumptions, the total mass flux of each species at the interface must vanish

$$j_{i,g}(I^+) + \dot{r}_{i,g}^{surf} = 0 \tag{13}$$

in which $\dot{r}_{i,g}^{surf}$ describes the surface flux due to surface reactions and the rate of destruction of reactive species i is characterized by the surface destruction efficiency γ_i (more details in[40]). This condition ensures that the diffusive flux from the gas phase toward the surface is exactly balanced by the rate of species consumption or production due to surface reactions, such that the net mass flux across the interface remains zero.

Energy Transport

With regard to energy transport, a conjugate heat transfer formulation[41] is adopted at the flame−material interface. Accordingly, two conditions are imposed to ensure a physically consistent thermal coupling between the gas phase and the solid material. First, temperature continuity is enforced at the interface, such that the temperature on the material side is equal to the temperature on the gas-phase side

$$T_g(I^+) = T_s(I^-) \tag{14}$$

Second, conservation of energy requires that the heat flux normal to the interface be continuous across the interface. This condition ensures that the conductive heat flux at the material side $j_{q,s}(I^-)$ exactly balances the total heat flux transferred from the flame side $j_{q,g}(I^+)$

$$j_{q,s}(I^-) = j_{q,g}(I^+) \tag{15}$$

$$j_{q,s}(I^-) = -\lambda_s \left.\frac{\partial T}{\partial z}\right|_{I^-} \tag{16}$$

$$j_{q,g}(I^+) = -\lambda_g \left.\frac{\partial T}{\partial z}\right|_{I^+} + \sum_{i=1}^{n_s} h_i j_{i,g}(I^+) \tag{17}$$

Gas Mixture and Chemical Mechanism

In the present study, a premixed stoichiometric CO/H_2/air unburnt gas mixture is considered, with an equimolar composition of CO and H_2 (CO/H_2 = 1:1). This specific fuel composition is selected as a representative example rather than a restrictive choice. The only requirement for the

https://doi.org/10.1021/acsomega.6c05832
ACS Omega XXXX, XXX, XXX−XXX

Table 1. Parameters for Representing Kinetic Coefficients as Functions of Temperature[34,a]

parameters	D_{per} [m^2/s]	D_{cor} [m^2/s]	$M_{per\text{-}sp}$ [$m^4/(Js)$]	$M_{sp\text{-}cor}$ [$m^4/(Js)$]
c_1	-5.1751×10^4	-5.9078×10^4	-5.1910×10^4	-1.0976×10^5
c_0	−1.5841	−2.5645	−12.6847	30.0881

[a]The cor represents Al_2O_3, per represents MgO, and sp represents spinel.

selection of gas mixture is that, under the applied flame strain rate, the resulting flame-induced temperature within the solid material remains below approximately 1800 K, ensuring that both periclase and corundum phases remain in the solid state throughout the process.

To simulate the combustion behavior of the premixed flame, the FFCM-1 chemical kinetic mechanism[42] is employed. This mechanism has been extensively validated for syngas combustion over a wide range of operating conditions and has been shown to reliably capture the thermo-kinetic characteristics of CO/H_2/air flames.

For the surface chemistry at the flame−material interface, the formulation follows the approach reported in ref 40 Six recombination and destruction reactions of reactive species occurring on the material surface are considered, namely the surface removal of O, H, OH, HO_2, H_2O_2 and CHO radicals, with the corresponding formation of stable gas-phase products

$$(S1)\quad O \xrightarrow{wall} 0.5O_2$$

$$(S2)\quad H \xrightarrow{wall} 0.5H_2$$

$$(S3)\quad OH \xrightarrow{wall} 0.5H_2O + 0.25O_2$$

$$(S4)\quad HO_2 \xrightarrow{wall} 0.5H_2O + 0.75O_2$$

$$(S5)\quad H_2O_2 \xrightarrow{wall} H_2O + 0.5O_2$$

$$(S6)\quad CHO \xrightarrow{wall} CO + 0.5H_2$$

These surface reactions account for the loss of reactive intermediates at the wall and their recombination into less reactive species, thereby influencing both species concentrations and the local energy transport near the interface. For all reactive species involved, a surface destruction efficiency of $\gamma_i = 1 \times 10^{-3}$ is assumed, consistent with the values adopted in.[40]

Numerical Simulation

Combustion Simulation. The numerical simulations of the strained premixed flame are performed using the in-house combustion code INSFLA, which has been extensively applied for the investigation of laminar premixed flame configurations under strained conditions.[15,16] The governing equations presented in[1−5] are solved in a fully coupled manner for species transport, momentum and energy conservation together with detailed chemical kinetics and transport processes.

For the temporal integration of the governing equations, INSFLA uses the semi-implicit extrapolation integrator LIMEX,[43] which is specifically designed for stiff differential-algebraic systems. The semi-implicit treatment enables stable and efficient time integration while accurately resolving the strong thermo-chemical coupling within the flame structure.

In addition, the numerical grid is dynamically adapted during the simulation procedure. The adaptive mesh refinement strategy automatically increases the local grid resolution in regions with steep gradients of thermo-kinetic quantities, such as temperature and species mass fractions. This self-adaptive grid treatment ensures that all relevant flame structures and transport processes are sufficiently resolved throughout the simulation domain while maintaining computational efficiency.

Solid-State Reaction Simulation. All material specific parameters such as diffusion and mobility coefficients are derived from ref 34 All the Gibbs energy values required for the numerical calculations of TEP have been directly informed from the CALPHAD database[34] via the FactSage software package[44] using information and coupling method introduced in ref 34 Substituting eqs 7 and 9−12 in eq 8, generates a set of equations, containing the solid-state kinetic variables, which are then solved at each time step with the MATLAB2023b solver vpasolve. Since, these kinetic variables in turn represent the rates for certain characterizing parameters of the system, the solutions from vpasolve, are used to update these parameters before proceeding to the calculations of the next time instant. Hence, an explicit Euler scheme has been implemented in this work to solve how the system evolves over time.

The diffusion coefficients D and the interface mobility coefficients M are both temperature dependent and approximated from the Arrhenius's type law as

$$\ln(D\text{or}M) = c_0 + \frac{c_1}{T} \tag{18}$$

in which c_0 and c_1 are parameters representing kinetic coefficients, which can be found in Table 1.

The coefficients U for vacancy generation/annihilation are assumed to be constant values for the considered temperature range, since the sensitivity analysis shows that the variation of U values has minor influence on the spinel growth.[34] According to,[34] the $U_{per\text{-}sp} = U_{sp\text{-}cor} = 1 \times 10^{-11}$ m^4/Js.

Validation of the Proposed Modeling Framework

Although the fully coupled flame-material interaction process investigated in the present work has not yet been validated experimentally as an integrated system, the individual submodels used in the framework have been independently validated in previous studies.

For the solid-state reaction model, the Thermodynamic Extremal Principle (TEP)-based framework adopted in the present work has already been systematically compared with experimental measurements for $MgO-Al_2O_3$ spinel formation in ref 34 In this study, the predicted spinel layer growth kinetics in terms of interface migration behavior and concentration evolution showed good agreement with experimental measurements under high-temperature conditions, showing the capability of the TEP-based formulation to capture the essential nonequilibrium kinetics of the solid-state reaction system.

Regarding the combustion model, the reacting-flow formulation used here is based on the two-parameter description of strained premixed flames proposed in.[26] The governing equations and numerical framework have been

https://doi.org/10.1021/acsomega.6c05832
ACS Omega XXXX, XXX, XXX−XXX

extensively validated in previous combustion studies against experimental data for canonical flame configurations, including laminar flame speed,[45,46] extinction limits[47,48] and strained flame structures.[26,49]

Therefore, although direct experimental validation of the present fully coupled flame−material interaction framework remains part of future work, both the combustion and the solid-state reaction submodels are individually based on previously validated and physically established formulations.

Thermal Control Strategy for Heating Process

Temperature Regimes. Figure 2 shows the axial temperature distributions of the coupled flame−material system for

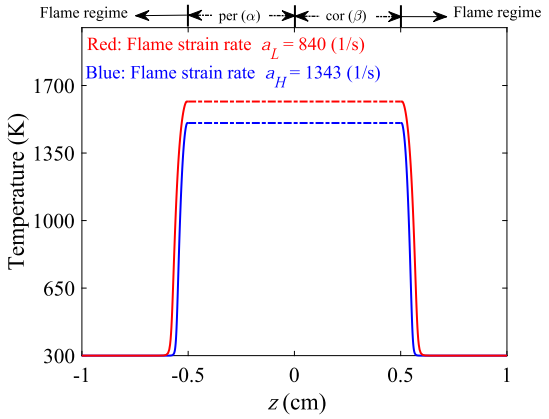

Figure 2. Flame temperature profiles with different imposed flame strain rate.

two different flame strain rates, showing how the thermal state of the material can be controlled through flame heating. The blue curve corresponds to the initial condition with a flame strain rate of a_H = 1343 s^{-1}, under which the flame maintains a relatively low temperature and imposes a "weak" thermal load on the solid (compared to the final flame temperature). As a result, the temperature inside the material is uniform at approximately 1505 K across both the periclase (MgO) layer and the corundum (Al_2O_3) layer. The red curve represents the heated state obtained after decreasing the flame strain rate to a_L = 840 s^{-1}. In this case, a noticeable increase in flame temperature is observed. Consequently, the internal temperature of the material increases to an average value of about 1620 K. This temperature increase is caused by the decrease in flame strain rate, which weakens convective transport and prolongs the residence time of reactive species within the high-temperature reaction zone, thereby enhancing the flame temperature.[50,51] These simple yet straightforward results indicate that decreasing the flame strain rate provides an effective and physically straightforward approach for regulating the internal temperature of the material during the heating process by adjusting only the flow conditions.

Temperature Homogeneity During Heating Process

To investigate how the rate of variation of the flame strain rate affects the homogeneity of the temperature distribution within the system, a controlled strain-rate modulation strategy is introduced. Specifically, the flame strain rate is assumed to decrease linearly from a higher value a_H to a lower value a_L, as shown in Figure 2, over a prescribed strain-rate transition time interval t_c as

$$a(t) = -\frac{a_H - a_L}{t_c}\cdot t + a_H \tag{19}$$

Under this formulation, a smaller value of t_c corresponds to a sharper and more rapid change in the flame strain rate, whereas a larger t_c represents a more slow change. By varying the value of t_c, different strain-rate ramping scenarios can be applied, allowing the transient evolution of the temperature field within the system to be systematically analyzed. This approach enables an assessment of how the heating process induced by variation of flame strain rate influences the development of temperature gradients and the degree of temperature homogeneity inside the material.

Figure 3 compares the temporal evolution of the material surface temperature (solid lines) and the maximum temperature inside the material (dashed lines) for different values of the strain-rate transition time t_c. For both cases, the heating process starts from the same initial temperature (due to the same imposed initial flame strain rate a_H = 1343 s^{-1}), while the subsequent thermal response strongly depends on the rate at which the flame strain rate is decreased to final imposed flame strain rate a_L = 840 s^{-1}. When a short transition time is applied, such as t_c = 5 min, a noticeable temperature difference develops between the material surface and its interior, indicating a highly inhomogeneous temperature distribution caused by the rapid increase of the flame temperature. As t_c increases, this temperature discrepancy diminishes clearly. For t_c = 20 min, the two temperature curves almost collapse onto each other, and no visible difference can be identified, indicating that the temperature field within the material is homogeneous under this condition. These results indicate that slower and smoother variations of the flame strain rate effectively reduce internal temperature gradients by allowing sufficient time for heat conduction within the solid. Based on this observation, any transition time t_c larger than 20 min can be considered sufficient to achieve a homogeneous temperature distribution inside the material. In practical applications, noticeable reactive diffusion process typically occurs over much longer time scales, often on the order of hours. Therefore, in the following analysis, a minimum transition time of t_c = 50 h is adopted. Consequently, a fully homogeneous temperature field throughout the material can be assumed.

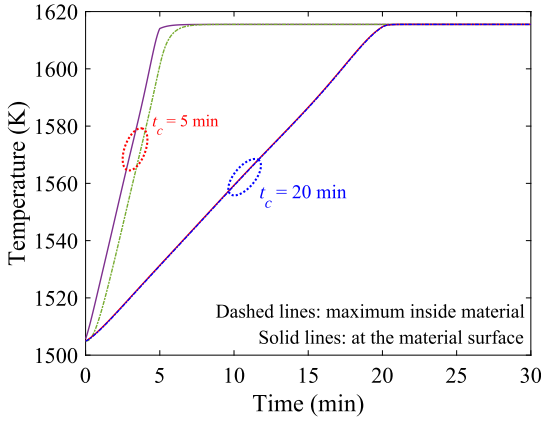

Figure 3. Comparison of temperature at the material surface and maximum temperature inside the material for three different cooling time t_c.

https://doi.org/10.1021/acsomega.6c05832
ACS Omega XXXX, XXX, XXX−XXX

Influence of Stochastic Variations in Flame Strain Rate on Material Temperature Evolution

In practical operating conditions, the flame strain rate is rarely perfectly smooth or deterministic, but may show stochastic fluctuations due to burner inlet perturbations or other possible external disturbances.[52] The present subsection investigates the influence of stochastic variations in the flame strain rate on the temperature evolution of the material. Specifically, a stochastic fluctuation term $a'(t)$ is superimposed onto the linear strain rate $a(t)$ considered previously via eq 19, allowing the flame strain rate to deviate randomly around its mean value. This approach enables an evaluation of whether noise in the flame strain rate can significantly affect the material temperature response and the homogeneity of the resulting temperature field. In this formulation, the temporal flame strain rate is expressed as $a_{st}(t) = a(t) + a'(t)$. The fluctuation term $a'(t)$ is assumed to follow a normal (Gaussian) distribution with a zero mean value and a standard deviation of $\sigma = 2.5\%$, which is adopted here as a representative example and observed from[52] for the measurement of flame strain rate. In addition, the amplitude of the stochastic fluctuation is limited to 10% of the instantaneous value of the linear strain rate $a(t)$, which is regarded as reasonable uncertainty in the experimental measurement for flame strain rate.[47,52] Under these assumptions, the temporal stochastic flame strain rate is defined as follows

$$a_{st} = a(t)\cdot(1 + 0.1\mathcal{N}(\mu = 0, \sigma = 2.5\%)) \quad (20)$$

Figure 4 illustrates the influence of stochastic variations in the flame strain rate on the thermal response of the material.

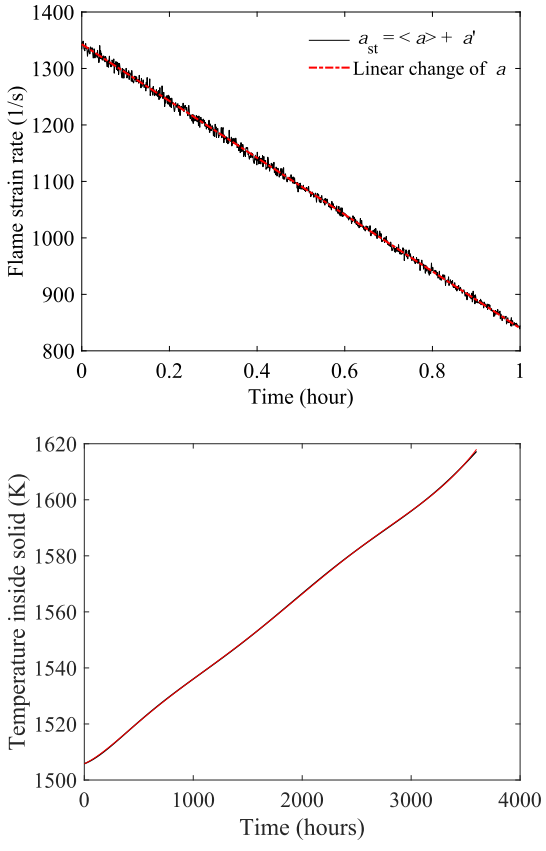

Figure 4. Upper: stochastic vs linear deterministic evolution of flame strain rate over 1 h time. Below: material temperature for both cases.

The upper subfigure compares the stochastic and the purely linear deterministic evolution of the flame strain rate over a time interval of 1 h. This duration is selected as a representative example, as it is sufficiently long to ensure a homogeneous temperature distribution within the material and to allow for the observation of spinel layer growth in the material. The lower subfigure shows the corresponding temporal evolution of the material temperature for both cases. Despite the presence of stochastic fluctuations in the flame strain rate, the temperature inside the material remains spatially homogeneous and closely follows the evolution associated with the mean value of the strain rate. This behavior indicates that fluctuations with high-frequency in the flame strain rate are effectively damped by the thermal inertia and slow heat conduction within the solid. As a result, the overall material temperature response is governed primarily by the averaged flame conditions rather than by instantaneous fluctuations, indicating the applicability of the proposed thermal control strategy against stochastic perturbations in the flame strain rate.

RESULTS AND DISCUSSION

The growth kinetics of the MAS phase formed via the solid-state reaction between MgO and Al_2O_3 are simulated in this work by implementing the TEP-based modeling framework introduced earlier. The thermal boundary conditions required as input for the kinetic model are obtained from the flame temperature calculations described previously. Three thermal loading scenarios are considered, in which the imposed strain rate decreases from $a_H = 1343\ s^{-1}$ to $a_L = 840\ s^{-1}$ (c.f. Figure 2) over transition time interval (t_c) of 50 h, 100 and 150 h, respectively. It should be mentioned that shorter transition times lead to only a few micrometer layer of the product phase due to the inherent slow solid state kinetics. Hence, for a representative growth-relevant analysis of the evolution characteristics of the spinel, conditions that allow longer exposure times for the material system to the flame have been selected. For each of the three transition time intervals investigated in this work, the material system experiences a heating profile from ∼1506 K to ∼1617 K as can be observed from Figure 3.

Thickness for Spinel Layer

Figure 5 shows the evolution of the spinel layer thickness during heating from approximately 1506 to 1617 K under different heating times. As observed, the most significant growth occurs for the longest transition time of 150 h (solid black line), reaching a final thickness of approximately 55.46 μm. This is followed by the case with a transition time of 100 h (solid blue line), which yields a comparable but slightly reduced thickness, while the shortest transition time of 50 h (solid red line) results in a significantly thinner spinel layer of approximately 32 μm. The reduced exposure duration associated with faster heating limits the available time for solid-state diffusion and interfacial reaction, thereby leading to a thinner product layer at any given temperature. Although the transition time represents a continuously varying thermal exposure rather than an isothermal hold, the nonlinear evolution of the spinel thickness over time within this temperature interval is characteristic of diffusion-controlled growth. It can however be observed from Figure 6 (upper), where the temperature dependence of the instantaneous spinel growth rate (time-derivative of thickness) is presented for each

https://doi.org/10.1021/acsomega.6c05832
ACS Omega XXXX, XXX, XXX−XXX

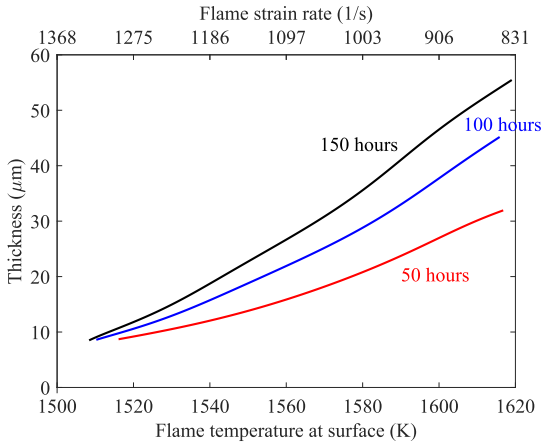

Figure 5. Thickness versus flame temperature at surface and versus flame strain rate for three different heating duration.

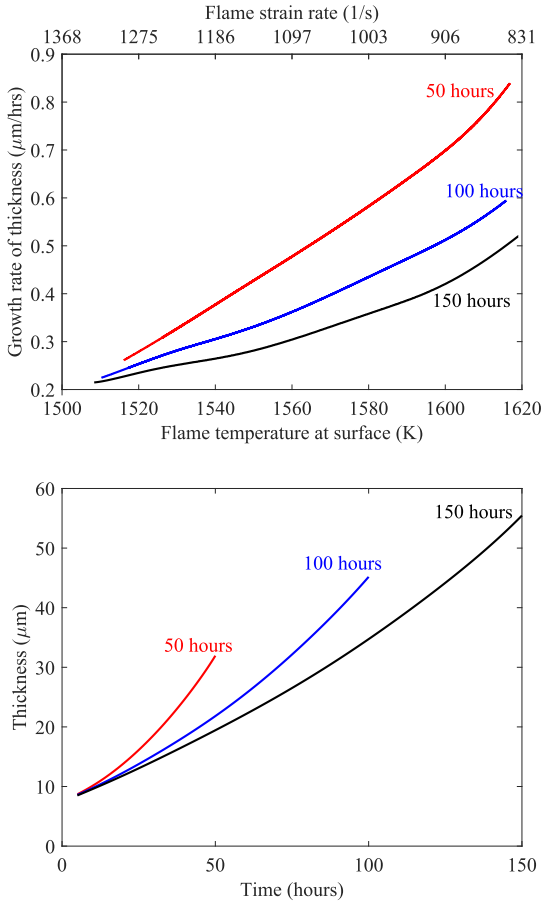

Figure 6. Upper: growth rate of spinel thickness over flame temperature and flame strain rate. Lower: growth of thickness over times. Both figures represent cases for three different heating times.

heating profile that the overall growth rate in each case, increases with temperature despite the increasing diffusion path length. This behavior is attributed to the strong temperature dependence of solid-state diffusion coefficients, which follow an Arrhenius-type relation and thus accelerate significantly at higher temperatures. Consequently, the temperature effect outweighs the increasing diffusion resistance within the investigated range. It should be noted that all heating profiles considered in the present study belong to a regime where the temperature-induced enhancement of diffusion and thermodynamic driving force dominates over the increasing diffusion length associated with spinel growth. Consequently, the instantaneous growth rate increases throughout the investigated heating process. A systematic identification of the transition to another regime, in which diffusion-path effects become dominant and the growth rate decreases with time, would require a much broader exploration of heating conditions and kinetic parameters. Such an investigation is beyond the scope of the present work, whose primary objective is to establish the coupled combustion−solid-state reaction framework and to investigate the influence of combustion-controlled thermal loading on spinel formation.

It can be further observed that, at any given temperature, the instantaneous growth rate of the faster heated system is consistently higher than that of the more slowly heated systems. Since the diffusion coefficient in the present framework is assumed to depend solely on temperature, this observation cannot be fully explained by temperature-dependent diffusivity alone. Therefore, the diffusion process must be further analyzed in terms of the available thermodynamic driving forces.

As reported in ref 53 increasing the temperature within the interval of approximately 1506 to 1617 K leads to a progressive expansion of the composition range of the thermodynamically stable spinel phase. Specifically, the stability region broadens from the stoichiometric composition (corresponding to 0.5 Al_2O_3) toward higher Al_2O_3 contents in equilibrium with the corundum interface and toward lower Al_2O_3 contents in equilibrium with the periclase interface. Consequently, at any given time instant, the faster heated system experiences a larger thermodynamic driving force for spinel formation. At the sp/cor interface, this promotes a pronounced Al_2O_3-enrichment in spinel compared to the slower heated systems. This calculated trend is consistent with the experimental analyses from ref 54 whereby increasing the temperature was shown to significantly increase the Al_2O_3 content of the spinel at the sp/cor interface. For the per/sp interface, even though there is a minor shift toward a more Al_2O_3-depleted spinel for the faster heated systems, the compositions remain close to the stoichimetreic composition as has been further experimentally observed in ref 54.

Thus, over the time interval during which all three profiles are still evolving, even though the spinel layer thickness of the faster heated system is more compared to the slowly heated systems as has been further illustrated in Figure 6 (lower subfigure), a faster diffusion is imposed by an overall steeper potential gradient across the spinel due to the faster interface composition evolutions compared to the slowly heated systems. This behavior can further be mapped from the evolution states of the system that have been represented in Figure 7 with the developing composition field within the spinel, as it grows from the solid state reaction over time for the three heating profiles. It can be observed that for any comparable time level (until 50 h), growth of the spinel layer thickness, along with its corresponding concentration gradient, is the maximum for the highest heating rate and lessens as the heating rate decreases. Conversely, for comparing the spinel characteristics for a particular temperature, the time levels for the systems with t_c = 100 and 150 h in Figure 7 should be chosen to be twice and thrice respectively to that for the system with t_c = 50 h. Under these conditions, it can be observed that even though faster heating yields lower

https://doi.org/10.1021/acsomega.6c05832
ACS Omega XXXX, XXX, XXX−XXX

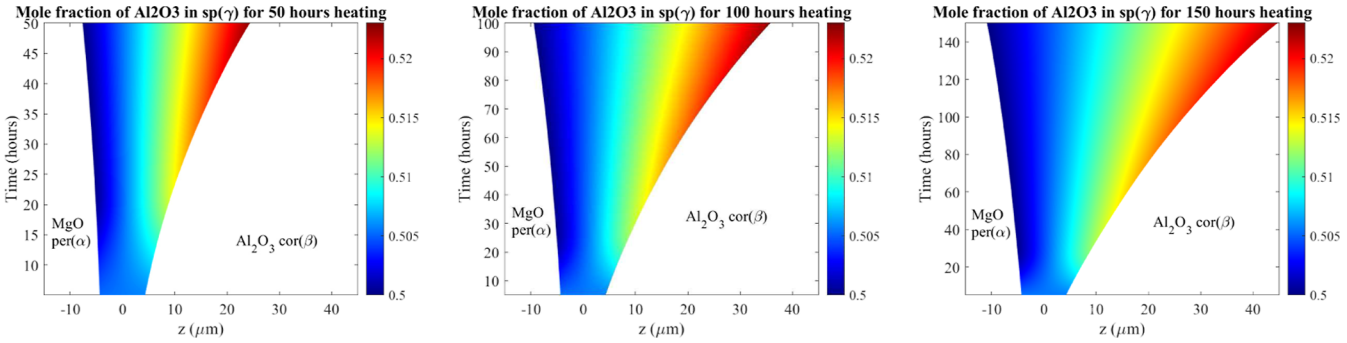

Figure 7. per/sp and sp/cor Interface movements and concentration evolution of spinel over time for three different heating duration.

thickness, the corresponding compositional spread within the spinel for the three systems are comparable. This further demonstrates the development of steeper potential gradient and the corresponding faster diffusion process that leads to higher growth rates at a particular temperature for the faster heated systems, as is depicted in Figure 6 (upper).

A further process relevant insight that can be extracted from these figures is that, depending on the objective of the manufacturing, whether to have a thicker product layer or a product with a comparatively more uniform composition distribution, the heat ramp applied to the system needs to be adjusted.

Partial Pressure of Oxygen and Water Vapor at the Ceramic Surface during Heating Process

For the fuel composition considered in this work, namely a premixed CO/H_2 mixture with CO/H_2 = 1:1 under stoichiometric conditions, complete combustion yields major products with molar proportions $H_2O/CO_2/N_2$ = 1:1:79/21. Compared to conventional hydrocarbon fuels, the presence of hydrogen in syngas leads to a relatively increased fraction of water vapor in the combustion products. As a consequence, during the heating process, the ceramic material is exposed not only to high temperatures but also to a steam- and oxygen-containing environment. Given that the thermal exposure durations investigated in this study range from 50 to 150 h, and may in practical applications extend even further, the material surface remains in long contact with high-temperature water vapor. Under such conditions, the possibility of surface oxidation cannot be excluded.[55−57]

Quantitative data on high-temperature oxidation or surface alteration for the specific material system considered here are limited. Therefore, the present section does not attempt to explicitly model oxidation kinetics but rather highlights this aspect as a potentially relevant phenomenon. A systematic investigation of surface oxidation effects under flame-controlled high-temperature steam and oxygen environments would constitute an important direction for future research.

Figure 8 presents the evolution of the partial pressures of O_2 and H_2O during the entire spinel growth process for the three investigated heating profiles at the material surface. Although the combustion system operates under stoichiometric conditions, a finite amount of molecular oxygen is still present in the burned gas. This residual O_2 originates from high-temperature thermodynamic equilibrium effects, where dissociation and recombination reactions lead to a nonzero equilibrium oxygen concentration. As shown in the upper subfigure, the partial pressure of O_2 remains relatively low, on the order of 0.08 bar, and decreases as the thermal history

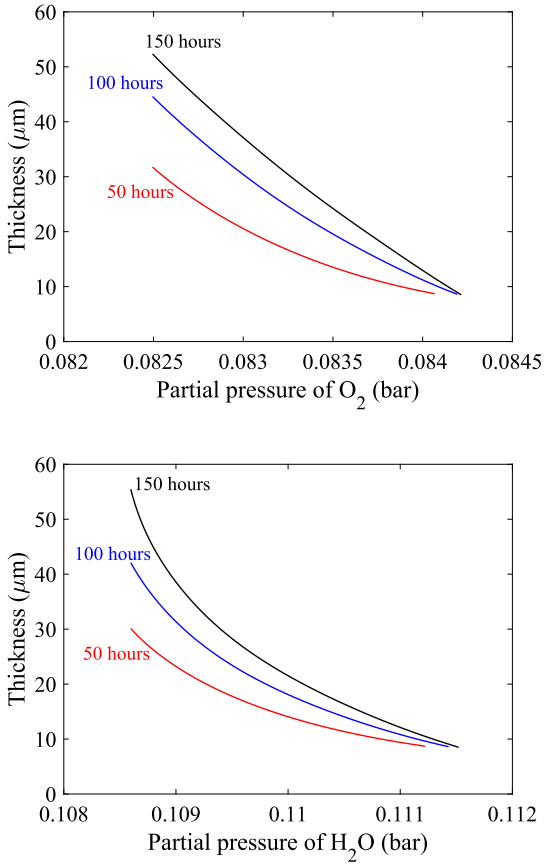

Figure 8. Evolution of the partial pressures of (upper) O_2 and (lower) H_2O at the material surface during spinel growth for heating times of 50 h, 100 and 150 h.

evolves. The partial pressure of H_2O, shown in the lower subfigure, is significantly higher, remaining around 0.11 bar throughout the process. This comparatively large steam fraction is a direct consequence of the hydrogen-containing syngas fuel. Given the prolonged exposure times considered in this work (up to 150 h), the material surface experiences sustained contact with a high-temperature oxygen- and steam-rich environment.

The finding suggests that for a more accurate predictive framework, the formation of oxidation layers at the MgO and Al_2O_3 surface need to be identified. Future models should incorporate coupled oxidation and solid-state reaction kinetics, supported by dedicated experimental investigations under controlled oxygen- and steam-containing combustion atmospheres.

https://doi.org/10.1021/acsomega.6c05832
ACS Omega XXXX, XXX, XXX−XXX

CONCLUSION

In the present work, a combustion-driven thermal engineering framework has been developed to investigate nonisothermal solid-state spinel formation in a $MgO-Al_2O_3$ system. By coupling a laminar strained premixed syngas/air flame model with a Thermodynamic Extremal Principle (TEP)-based solid-state kinetic model, a direct link between controllable combustion parameters and solid-state reaction has been coupled and studied.

The results showed that modulation of the imposed flame strain rate provides a physically straightforward and efficient strategy for regulating the thermal loading of the material. A decrease in strain rate leads to a predictable increase in flame temperature and, consequently, in the homogeneous internal temperature of the ceramic system. It has been shown that sufficiently slow strain-rate transitions ensure spatially uniform temperature distributions within the material, thereby enabling well-defined nonisothermal reaction conditions over prolonged heating durations.

The spinel growth kinetics have been characterized based on both the thickness and composition evolution of the interphase as a function of the applied thermal loading. Faster heating profiles, although associated with shorter overall reaction times and thinner final product layers, show higher instantaneous growth rates. This behavior results from the combined effects of enhanced temperature-dependent transport kinetics, through increased diffusion coefficients, and steeper thermodynamic driving forces arising from the expansion of the spinel stability region at elevated temperatures. These findings suggest the importance of considering both transport and thermodynamic-driving force when describing diffusion-controlled solid-state transformations under transient thermal conditions.

Furthermore, stochastic fluctuations in the flame strain rate have been shown to exert negligible influence on the material temperature evolution, owing to the thermal inertia of the solid. This finding indicates that the proposed combustion-based thermal control strategy is robust against realistic operating disturbances.

Finally, the analysis of the combustion product atmosphere showed sustained exposure of the material surface to elevated partial pressures of H_2O and finite O_2 concentrations, whose aspect highlights the necessity of incorporating coupled oxidation−diffusion phenomena into future modeling efforts.

Although the present one-dimensional formulation provides a suitable framework for investigating the coupling between combustion-controlled heating and solid-state reaction kinetics, radial heat transfer and temperature nonuniformities may become important in practical systems with finite lateral dimensions or thicker materials. Future work will therefore focus on extending the present methodology to a higher dimensional coupled flame-material model, enabling the prediction of spatial variations in spinel growth and a more realistic description of combustion-assisted processing.

AUTHOR INFORMATION

Corresponding Author

Chunkan Yu − *Institute of Technical Thermodynamics, Karlsruhe Institute of Technology, 76131 Karlsruhe, Germany*; orcid.org/0000-0002-0550-5003; Phone: +49 721 608 43996; Email: chunkan.yu@kit.edu; Fax: +49 721 608 43931

Authors

Sanchita Chakrabarty − *Institute of Technical Thermodynamics, Karlsruhe Institute of Technology, 76131 Karlsruhe, Germany*

Michael Fischlschweiger − *Institute of Technical Thermodynamics, Karlsruhe Institute of Technology, 76131 Karlsruhe, Germany*

Complete contact information is available at: https://pubs.acs.org/10.1021/acsomega.6c05832

Notes

The authors declare no competing financial interest.

ACKNOWLEDGMENTS

Financial funded by the DFG project H2MAT3D(project number 523879740 within the DFG-SPP 2419) and by the DFG project (project number 470323858 within the DFG-SPP 2315).

REFERENCES

(1) Linke, J.; Akiba, M.; Duwe, R.; Lodato, A.; Penkalla, H.-J.; Rödig, M.; Schöpflin, K. Material degradation and particle formation under transient thermal loads. *J. Nucl. Mater.* **2001**, *290*, 1102−1106.

(2) Stathopoulos, N.; Belessiotis, G.; Oikonomou, P.; Papanicolaou, E. Experimental investigation of thermal degradation of phase change materials for medium-temperature thermal energy storage and tightness during cycling inside metal spheres. *J. Energy Storage* **2020**, *31*, 101618.

(3) Hasanuzzaman, M.; Rahim, N.; Hosenuzzaman, M.; Saidur, R.; Mahbubul, I.; Rashid, M. M. Energy savings in the combustion based process heating in industrial sector. *Renewable Sustainable Energy Rev.* **2012**, *16*, 4527−4536.

(4) Gao, Q.; Pang, Y.; Sun, Q.; Liu, D.; Zhang, Z. Numerical analysis of the heat transfer of radiant tubes and the slab heating characteristics in an industrial heat treatment furnace with pulse combustion. *Int. J. Therm. Sci.* **2021**, *161*, 106757.

(5) Baukal, J.; Gershtein, V.; Li, X. J. *Computational fluid dynamics in industrial combustion*; CRC Press, 2000.

(6) Roozeboom, F.; Parekh, N. Rapid thermal processing systems: A review with emphasis on temperature control. *J. Vac. Sci. Technol., B:Microelectron. Process. Phenom.* **1990**, *8*, 1249−1259.

(7) Yang, M.; Zhong, H.; Li, T.; Wu, B.; Wang, Z.; Sun, D. Phase change material enhanced radiative cooler for temperature-adaptive thermal regulation. *ACS Nano* **2023**, *17*, 1693−1700.

(8) Xing, W.; Xu, Y.; Song, C.; Deng, T. Recent advances in thermal interface materials for thermal management of high-power electronics. *Nanomaterials* **2022**, *12*, 3365.

(9) Liu, L.; Tang, Y.; Liu, D. Investigation of future low-carbon and zero-carbon fuels for marine engines from the view of thermal efficiency. *Energy Rep.* **2022**, *8*, 6150−6160.

(10) Cardoso, J. S.; Silva, V.; Rocha, R. C.; Hall, M. J.; Costa, M.; Eusébio, D. Ammonia as an energy vector: Current and future prospects for low-carbon fuel applications in internal combustion engines. *J. Cleaner Prod.* **2021**, *296*, 126562.

(11) Kohse-Hoöinghaus, K. Combustion, chemistry, and carbon neutrality. *Chem. Rev.* **2023**, *123*, 5139−5219.

(12) Egolfopoulos, F. N. Dynamics and structure of unsteady, strained, laminar premixed flames. *Symp. (Int.) Combust.* **1994**, *25*, 1365−1373.

(13) Petrov, C. A.; Ghoniem, A. F. The transient response of strained laminar-premixed flames. *Combust. Flame* **1995**, *102*, 401−417.

(14) Wang, S.; Wang, Z.; Roberts, W. L. Measurements and simulations on effects of elevated pressure and strain rate on NOx emissions in laminar premixed NH3/CH4/air and NH3/H2/air flames. *Fuel* **2024**, *357*, 130036.

(15) Yu, C.; Böhlke, T.; Valera-Medina, A.; Yang, B.; Maas, U. Flame−Solid interaction: Thermomechanical analysis for a steady laminar stagnation flow stoichiometric nh3−h2 flame at a plane wall. *Energy Fuels* **2023**, *37*, 3294−3306.
(16) Yu, C.; Srikanth, S.; Böhlke, T.; Gorr, B.; Maas, U. Steady laminar stagnation flow NH3-H2-air flame at a plane wall: Flame extinction limit and its influence on the thermo-mechanical stress and corrosive behavior of wall materials. *Appl. Energy Combust. Sci.* **2024**, *18*, 100261.
(17) Noor, M.; Wandel, A. P.; Yusaf, T. MILD combustion: the future for lean and clean combustion technology. *Int. Rev. Mech. Eng.* **2014**, *8*, 251−257.
(18) Kohse-Höinghaus, K. Clean combustion: Chemistry and diagnostics for a systems approach in transportation and energy conversion. *Prog. Energy Combust. Sci.* **2018**, *65*, 1−5.
(19) Maksimov, V.; Welch, R. S.; Potter, A. R.; Rimsza, J. M.; Mauro, J. C.; Wilkinson, C. J. Role of water in fracture of modified silicate glasses. *J. Am. Ceram. Soc.* **2024**, *107*, 7727−7738.
(20) Lin, H.; Yao, X.; Wang, X.; Zhang, X.; Mao, H.; Zhang, J.; Li, X.; Shu, Y.; Vujanovic, M.; Mikulčić, H. Green ammonia co-firing in cement rotary kiln: numerical investigation on clinker quality and NOx emission by gas−solid interaction. *Appl. Therm. Eng.* **2025**, *277*, 127116.
(21) Aksel, C.; Rand, B.; Riley, F. L.; Warren, P. D. Mechanical properties of magnesia-spinel composites. *J. Eur. Ceram. Soc.* **2002**, *22*, 745−754.
(22) Baudín, C.; Martínez, R.; Pena, P. High-temperature mechanical behavior of stoichiometric magnesium spinel. *J. Am. Ceram. Soc.* **1995**, *78*, 1857−1862.
(23) Rodriguez-Suarez, T.; Lopez-Esteban, S.; Bartolomé, J.; Moya, J. Mechanical properties of alumina-rich magnesium aluminate spinel/tungsten composites. *J. Eur. Ceram. Soc.* **2007**, *27*, 3339−3344.
(24) Shamim, M.; Sinhamahapatra, S.; Hossain, J.; Lahiri, S.; Dana, K. Kinetic analysis of magnesium aluminate spinel formation: Effect of MgO: Al2O3 ratio and titania dopant. *Ceram. Int.* **2018**, *44*, 1868−1874.
(25) Abart, R.; Svoboda, J.; Ječabek, P.; Povoden-Karadeniz, E.; Habler, G. Interlayer growth kinetics of a binary solid-solution based on the thermodynamic extremal principle: application to the formation of spinel at periclase-corundum contacts. *Am. J. Sci.* **2016**, *316*, 309−328.
(26) Stahl, G.; Warnatz, J. Numerical investigation of time-dependent properties and extinction of strained methane- and propane-air flamelets. *Combust. Flame* **1991**, *85*, 285−299.
(27) Arrhenius, S. Über die Dissociationswärme und den Einfluss der Temperatur auf den Dissociationsgrad der Elektrolyte. *Z. Phys. Chem.* **1889**, *4U* (4), 96−116.
(28) Warnatz, J.; Maas, U.; Dibble, R. W. *Combustion: physical and chemical fundamentals, modeling and simulation, experiments, pollutant formation*; Springer: Berlin Heidelberg, 2006.
(29) Turns, S. R. *Introduction to combustion*; McGraw-Hill Companies: New York, NY, USA, 1996; Vol. *287*.
(30) Hirschfelder, J. O.; Curtiss, C. F.; Bird, R. B.; Mayer, M. G. *Molecular theory of gases and liquids*; Wiley New York, 1964; Vol. *165*.
(31) Acquaviva, M. R.; Porcarelli, A.; Langella, I. Influence of Soret effect on flame structure and NOx emissions in highly strained lean premixed counterflow hydrogen flames. *Fuel* **2025**, *395*, 134939.
(32) Egolfopoulos, F. Geometric and radiation effects on steady and unsteady strained laminar flames. *Symp. (Int.) Combust.* **1994**, *25*, 1375−1381.
(33) Vance, F. H.; de Goey, P.; van Oijen, J. A. The effect of thermal diffusion on stabilization of premixed flames. *Combust. Flame* **2020**, *216*, 45−57.
(34) Chakrabarty, S.; Li, H.; Fischlschweiger, M. Calphad-informed thermodynamic non-equilibrium simulation of non-isothermal solid-state reactions of magnesium aluminate spinel based on the thermodynamic extremal principle. *Materialia* **2023**, *28*, 101723.
(35) Svoboda, J.; Gamsjäger, E.; Fischer, F. D.; Liu, Y.; Kozeschnik, E. Diffusion processes in a migrating interface: The thick-interface model. *Acta Mater.* **2011**, *59*, 4775−4786.
(36) Svoboda, J.; Turek, I.; Fischer, F. D. Application of the thermodynamic extremal principle to modeling of thermodynamic processes in material sciences. *Philos. Mag.* **2005**, *85*, 3699−3707.
(37) Götze, L. C.; Abart, R.; Rybacki, E.; Keller, L. M.; Petrishcheva, E.; Dresen, G. Reaction rim growth in the system MgO-Al2O3-SiO2 under uniaxial stress. *Mineral. Petrol.* **2010**, *99*, 263−277.
(38) Gamsjäger, E.; Liu, Y.; Rester, M.; Puschnig, P.; Draxl, C.; Clemens, H.; Dehm, G.; Fischer, F. D. Diffusive and massive phase transformations in Ti−Al−Nb alloys−Modelling and experiments. *Intermetallics* **2013**, *38*, 126−138.
(39) Svoboda, J.; Turek, I. On diffusion-controlled evolution of closed solid-state thermodynamic systems at constant temperature and pressure. *Philos. Mag. B* **1991**, *64*, 749−759.
(40) Maas, U.; Warnatz, J. Ignition processes in carbon-monoxide-hydrogen-oxygen mixtures. *Symp. (Int.) Combust.* **1989**, *22*, 1695−1704.
(41) He, L. Conjugate heat transfer: Some fundamentals and recent progress. *Adv. Heat Transfer* **2023**, *55*, 41−87.
(42) Foundational Fuel Chemistry Model Version 1.0 (FFCM-1). 2016. https://web.stanford.edu/group/haiwanglab/FFCM1/pages/FFCM1.html (accessed 12 30, 2021).
(43) Deuflhard, P.; Nowak, U. *Large Scale Scientific Computing*; Springer, 1987; pp 37−50.
(44) Bale, C. W.; Bélisle, E.; Chartrand, P.; Decterov, S. A.; Eriksson, G.; Gheribi, A. E.; Hack, K.; Jung, I.-H.; Kang, Y.-B.; Melancon, J.; et al. Reprint of: FactSage thermochemical software and databases, 2010−2016. *CALPHAD* **2016**, *55*, 1−19.
(45) Razus, D.; Oancea, D.; Brinzea, V.; Mitu, M.; Movileanu, C. Experimental and computed burning velocities of propane−air mixtures. *Energy Convers. Manage.* **2010**, *51*, 2979−2984.
(46) Kuznetsov, M.; Redlinger, R.; Breitung, W.; Grune, J.; Friedrich, A.; Ichikawa, N. Laminar burning velocities of hydrogen-oxygen-steam mixtures at elevated temperatures and pressures. *Proc. Combust. Inst.* **2011**, *33*, 895−903.
(47) Eckart, S.; Yu, C.; Maas, U.; Krause, H. Experimental and numerical investigations on extinction strain rates in non-premixed counterflow methane and propane flames in an oxygen reduced environment. *Fuel* **2021**, *298*, 120781.
(48) Eckart, S.; Yu, C.; Lin, S.; Maas, U.; Krause, H.; Yang, B. An experimental and modeling study on extinction strain rate in C2HX flames with varied oxygen content. *J. Energy Inst.* **2024**, *116*, 101702.
(49) Prabasena, B.; Röder, M.; Kathrotia, T.; Riedel, U.; Dreier, T.; Schulz, C. Strain rate and fuel composition dependence of chemiluminescent species profiles in non-premixed counterflow flames: comparison with model results. *Appl. Phys. B:Lasers Opt.* **2012**, *107*, 561−569.
(50) Sun, C.; Sung, C.; Law, C. K. Response of counterflow premixed and diffusion flames to strain rate variations at reduced and elevated pressures. *Symp. (Int.) Combust.* **1996**, *26*, 1111−1120.
(51) Zhou, R.; Hochgreb, S. The behaviour of laminar stratified methane/air flames in counterflow. *Combust. Flame* **2013**, *160*, 1070−1082.
(52) Richter, M.; Schultheis, R.; Dawson, J.; Gruber, A.; Barlow, R.; Dreizler, A.; Geyer, D. Extinction strain rates of premixed ammonia/hydrogen/nitrogen-air counterflow flames. *Proc. Combust. Inst.* **2023**, *39*, 2027−2035.
(53) Zienert, T.; Fabrichnaya, O. Thermodynamic assessment and experiments in the system MgO−Al2O3. *CALPHAD* **2013**, *40*, 1−9.
(54) Watson, E. B.; Price, J. D. Kinetics of the reaction MgO+ Al2O3 → MgAl2O4 and Al-Mg interdiffusion in spinel at 1200 to 2000° C and 1.0 to 4.0 GPa. *Geochim. Cosmochim. Acta* **2002**, *66*, 2123−2138.
(55) Lee, K. N.; Garg, A.; Jennings, W. Effects of the chemistry of coating and substrate on the steam oxidation kinetics of environmental barrier coatings for ceramic matrix composites. *J. Eur. Ceram. Soc.* **2021**, *41*, 5675−5685.

https://doi.org/10.1021/acsomega.6c05832
ACS Omega XXXX, XXX, XXX−XXX

(56) Jacobson, N. S.; Opila, E. J.; Lee, K. N. Oxidation and corrosion of ceramics and ceramic matrix composites. *Curr. Opin. Solid State Mater. Sci.* **2001**, *5*, 301−309.
(57) Hou, X.-M.; Chou, K.-C. Quantitative interpretation of the parabolic and nonparabolic oxidation behavior of nitride ceramic. *J. Eur. Ceram. Soc.* **2009**, *29*, 517−523.

https://doi.org/10.1021/acsomega.6c05832
ACS Omega XXXX, XXX, XXX−XXX